

A CT Image-Based Virtual Sensing Method to Estimate Bone Drilling Force for Surgical Robots

Liang Li , Sheng Yang , Wuke Peng, Hui Ding, *Member, IEEE*, and Guangzhi Wang , *Member, IEEE*

Abstract—Objective: Current surgical robots face challenges to understand preoperative images like human surgeons, which hindering robots from making full use of preoperative information to operate stably and efficiently. We offer a method to estimate drilling force information based on preoperative images to provide a priori force information for surgical robots performing bone drilling tasks. **Methods:** A visual sensing computing framework is proposed to help robots calculate drill-tissue contact area 3D image information in a one-dimensional signal format. Under this computing framework, a computed tomography (CT) image-weighted bone drilling mechanical model is built, which further considers both targets bone shape and material properties to predict the thrust force, torque, and radial force of a drilling process based on preoperative CT images. **Results:** The built model can respond to multiple bone drilling process factors, such as personalized surgery plans, varying tissue densities, uneven drilling surfaces, different drilling speeds, feed rates, and drill bit geometries. The best trust force prediction error on bovine bones is 1.13 ± 0.95 N, and the best normalized average prediction error on porcine bones is 0.07 ± 0.08 . Experiments in spinal pedicle screw placement surgery also show potential application abilities. **Conclusion:** Our method predicts the bone drilling force well based on preoperative images, providing robots with more efficient preoperative information. **Significance:** This work offers a new perspective to study the interaction relationship between robot surgical instruments and tissues with the assistance of preoperative images.

Index Terms—Operational state prediction, surgery robot, medical image, force situation awareness, virtual sensing.

I. INTRODUCTION

ONE drilling is a common surgical procedure [1]. How to make robots realize safe and autonomous bone drilling procedures is an urgent clinical need. For example, in neurosurgical

Manuscript received April 6, 2021; revised July 21, 2021; accepted August 21, 2021. Date of publication August 30, 2021; date of current version January 20, 2022. This work was supported in part by National Nature Science Foundation of China under Grant U20A20389, in part by the Beijing Municipal Science & Technology Commission under Grants Z191100007619036 and L192046, and in part by the Tsinghua University Initiative Scientific Research Program under Grant 20197010009. (*Corresponding author: Guangzhi Wang*)

Liang Li, Sheng Yang, Wuke Peng, and Hui Ding are with the Department of Biomedical Engineering, School of Medicine, Tsinghua University, China.

Guangzhi Wang is with the Department of Biomedical Engineering, School of Medicine, Tsinghua University, Beijing 100084, China (e-mail: wgz-dea@tsinghua.edu.cn).

Digital Object Identifier 10.1109/TBME.2021.3108400

interventions, a “burr hole” channel must be drilled into the skull for instruments to reach the intracranial brain area [2]. In pedicle screw placement operations, it is also necessary to predrill a channel on an uneven vertebral surface to ensure accurate screw placement [3]. Although current stereotactic surgical robots can already accurately determine drilling position and direction [3] and [4], the final feeding operation still needs to be manually completed. Surgeons need to be extremely careful not only to push the drill tool forward to reach the predetermined drilling depth but also to be ready to withdraw at any time to prevent accidental outcomes, such as drill breakthrough, overshoot, slippage, and breakage, from damaging the brain tissue, spinal cord, and other key anatomical structures.

A bone drilling procedure is usually carried out under minimally invasive conditions, and it is difficult to directly observe the interaction state between the drill bit and the bone. Researchers have deployed various sensor devices to monitor bone drilling status, aiming to establish connections between the sensor signal and the bone drilling status to help robots evaluate the minimally invasive drilling status in real-time. The drilling force is the most direct signal that reflects the drilling interaction state. Research on robot drilling status identification using force sensors was initially conducted, and the results are extensive [5]–[7]. In addition, various real-time information, such as sound [8], [9], vibration [10], and even drill motor power [11], [12], has been used to recognize the bone cutting or drilling status. The real-time sensor information instantly reflects the current operating status and allows rapid robot response. However, this requires a very accurate and reliable state identification model. Patient anatomical structures vary, as do tissue lesion properties. Faced with these unstructured factors, there is considerable risk in identifying the robot drilling status by relying entirely on a real-time status recognition model.

Preoperative images help surgeons determine the anatomical structure before surgery. Can the robot also use these preoperative images to obtain some prior information and know what will happen before the actual drilling procedure? The grayscale of computed tomography (CT) images (Hounsfield units, HU) is directly related to the density of bone tissue [13], [14]. Experimental research has further found that bone tissue strength and stiffness have a power relationship with bone density [15]. This means that there are some correlations between the bone-instrument interaction force information and CT images of bone tissue. However, how to better establish these correlations still needs to be explored. Jin *et al.* [16] extracted CT bone tissue images as point clouds, aiming to use the point

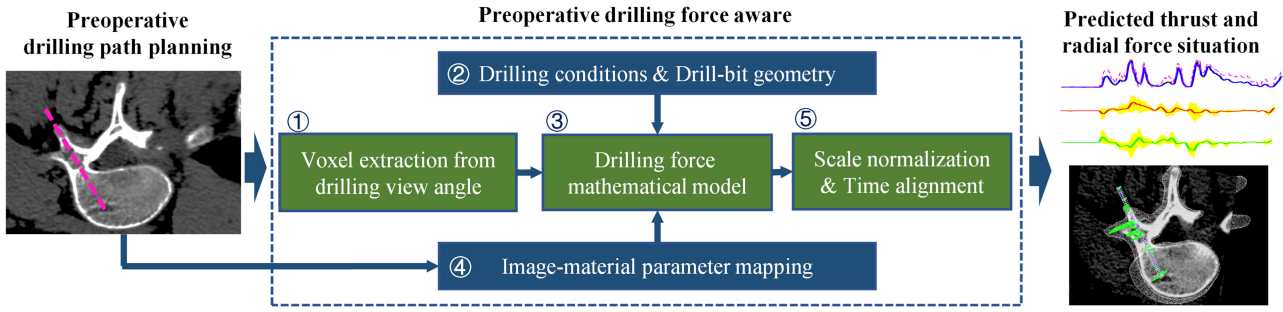


Fig. 1. Framework of image-based robot preoperative drilling force estimation.

cloud density information on the drilling path to build a model to predict the thrust force for the robot drilling process. Williamson *et al.* assumed that the grayscale of the CT image on the robot drilling path was directly related to the drilling thrust force [17]. They also used this idea to help the robot further predict the drilling temperature on the drilling path [18]. Despite these preliminary works, these existing models do not consider the real action mechanism between drilling tools and bone tissue, and from the results of these published works, the prior drilling force information obtained from the images does not seem to be consistent with actual measurements.

Drilling force models have been studied in the field of metal manufacturing for many years [19]–[21]. The experimental results have shown that models describing metal drilling are also effective for the bone drilling process [22], [23]. Related researches on bone drilling mechanical models have mostly focused on cortical bones (tibia) with singular material characteristics [5], [6], [12], [22], [24]. However, in an actual drilling process, the drill bit interacts with tissues with various material characteristics, such as cortical bone, cancellous bone, and bone marrow. Due to the multiple material properties and complex material structures involved, this process still lacks accurate model descriptions. Moreover, the real bone structures in clinical surgery rarely have a smooth, nearly ideal vertical drilling surface like the tibia. For uneven bone surfaces such as vertebrae, lateral force or even slippage may occur during the drill bit entry process. There is a lack of models that describe this kind of phenomenon.

In this work, we take robot bone drilling as an example to provide a perspective for robot observe and calculate the preoperative images to obtain prior drilling force state information. A CT density images-based tool-image interaction model was established, which can predict the robot drilling force state. A calculation method for lateral drilling force was also provided for drilling on an uneven bone surface.

II. METHODS

A. Method Overview

CT images reflect the bone shape and tissue material density information well. In this work, the robot drilling process is first mapped to the image space, which is regarded as the interaction process between the drill cutting edge geometric model and the image voxel of the local cutting object on the planned path. Then, inspired by the concept of virtual sensors, an image-based virtual

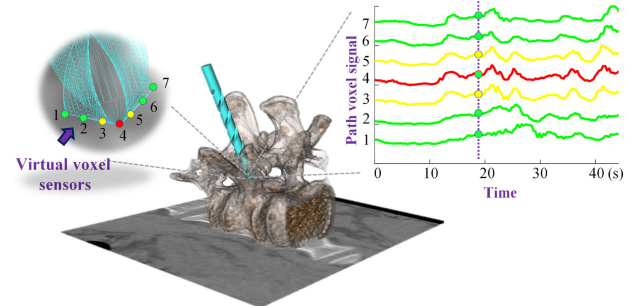


Fig. 2. Voxel signal from the drilling path based on the virtual sensor method.

sensing framework is built to process the interaction area image information in sensor signal format. Finally, a mechanical model of the drilling process model is introduced to establish the sensor transfer function from the image signal to the predicted drilling force signal.

The method framework is designed as shown in Fig. 1. Five modules are included: Module ① extracts the CT voxel signal from the drill path area. This signal contains both the material and geometric information of the drill target. Module ② is used to calculate drilling conditions and drill bit geometry information. Module ③ constructs a mathematical model to predict drilling force information. Module ④ is used to map CT images to tissue material characteristic parameters. All the above information is input into module ③ to calculate the drilling thrust force, torque, and lateral force information. Finally, module ⑤ performs amplitude standardization and time alignment on the predicted force data, making it standardized and comparable.

B. Image-Based Virtual Sensing Framework

The concept of the image-based virtual sensing method is shown in Fig. 2. Imagine that a series of virtual sensors are installed on the drill bit. When the bit drills through the bone anatomical structure in the image space according to the surgical plan, these virtual sensors can sense the contacted image voxel value signal at the current location. These signals are then processed by an appropriate transfer function and output as the target sensor signal output. The mathematical model of the

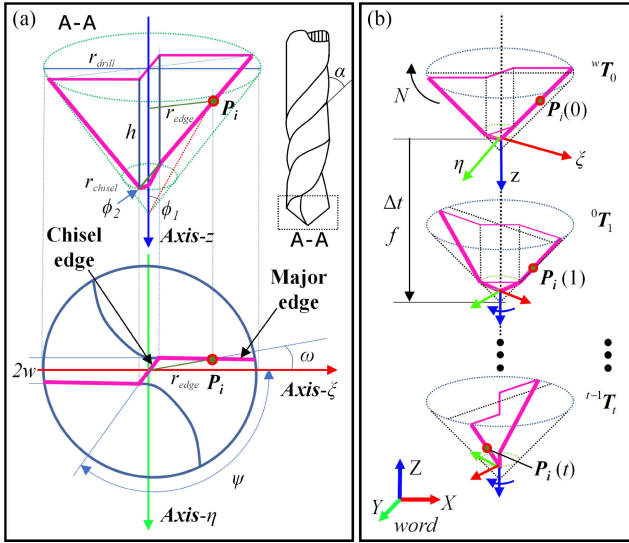


Fig. 3. Geometric model of the drill bit cutting edge. (a) Static geometric model. (b) Dynamic model when drill motion.

virtual sensor can be represented by (1).

$$y^i(t) = \text{func}(\mathbf{I}(\mathbf{P}_i(t))) \quad (1)$$

where $y^i(t)$ is the signal output by the i th sensor at time t , $\mathbf{P}_i(t)$ is the position of the i th sensor at time t , \mathbf{I} is the image voxel value corresponding to the sensor position, and func is the transfer function of the voxel value.

The above virtual sensing method allows us to treat high-dimensional 3D image information as one-dimensional signals. More importantly, this method helps obtain the contact information between surgical instruments and anatomical structures in the image space. When virtual sensors are installed on the cutting edge of the drill, the sensed image signals actually contain the drill-tissue contact information of different bone tissue shapes and density characteristics at the cutting area. If the transfer function from the image signal to the cutting force can be established, we can infer the contact force information between the drill bit and the anatomical structure during the drilling process.

C. Morphological and Kinematic Models of the Drill Bit

In Equation (1), the coordinate position $\mathbf{P}_i(t)$ of the virtual sensor is one of the indispensable inputs. Here, a widely used orthopedic twist drill is selected as the drilling tool in this research. Considering that the major and chisel edges play the main role during bone drill cutting, a morphological and drilling process kinematic model of the drill bit major and chisel edges is built. With these models, the coordinate position $\mathbf{P}_i(t)$ of each virtual sensor can be derived. Then, the image voxel signals \mathbf{I} can further be indexed in image space according to the position $\mathbf{P}_i(t)$.

1) Morphological Model of Drill Cutting Edge: Fig. 3(a) reveals the geometrical description of the cutting edge in the static state. In the drill coordinate $\xi\text{-}\eta\text{-}z$, \mathbf{P}_i (a point i in the drill's cutting edge) can be determined by (2). Here, \mathbf{P}_i is a function of the target point radial distance r_{edge} (ψ is the drill

chisel edge angle, ϕ_2 is the half drill chisel edge point angle, $\omega = \arcsin(w/r_e)$ is the projection of the oblique angle, w is the half drill web thickness, ϕ_1 is the half drill point angle, r_{chisel} is the drill chisel radius, and r_{drill} is the drill bit radius.

$$\begin{aligned} \mathbf{P}_i &= \begin{bmatrix} \xi_i \\ \eta_i \\ z_i \end{bmatrix} \\ &= \begin{cases} \begin{bmatrix} r_{edge}^i \cdot \cos(\pi - \psi) \\ r_{edge}^i \cdot \sin(\pi - \psi) \\ r_{edge}^i / \tan \phi_2 \end{bmatrix} & \text{if } 0 \leq r_{edge}^i < r_{chisel} \\ \begin{bmatrix} r_{edge}^i \cdot \cos(\omega) \\ -w \\ r_{edge}^i / \tan \phi_1 - r_{chisel} / (\tan \phi_1 - \tan \phi_2) \end{bmatrix} & \text{if } r_{chisel} \leq r_{edge}^i < r_{drill} \end{cases} \end{aligned} \quad (2)$$

2) Kinematic Model of the Drilling Process: The cutting motion of the drill is composed of feed and rotation around the Z-axis of its coordinate frame. As a result, the motion trajectory $\mathbf{P}_i(t)$ is a space spiral function of time t . By assuming the drill bit rotation speed is N and the feed rate is f_r . The motion transformation matrix of drill bit from time $t-1$ to t can be determined by (3). Here, $\Delta Ro = (2\pi N/60) \cdot \Delta t$ is the rotation angle around the Z_{t-1} -axis in time interval Δt and $\Delta Tr = (f_r N/60) \cdot \Delta t$ is the feed distance along the Z_{t-1} -axis in time interval Δt . Consequently, the motion trajectory of one virtual sensor $\mathbf{P}_i(t)$ can be determined by (4).

$$\begin{aligned} {}^{t-1}\mathbf{T}_t &= \underbrace{\begin{bmatrix} \cos(\Delta Ro) & -\sin(\Delta Ro) & 0 & 0 \\ \sin(\Delta Ro) & \cos(\Delta Ro) & 0 & 0 \\ 0 & 0 & 1 & 0 \\ 0 & 0 & 0 & 1 \end{bmatrix}}_{\text{Rotation around } Z_{t-1} \text{ axis}} \cdot \\ &\quad \underbrace{\begin{bmatrix} 1 & 0 & 0 & 0 \\ 0 & 1 & 0 & 0 \\ 0 & 0 & 1 & \Delta Tr \\ 0 & 0 & 0 & 1 \end{bmatrix}}_{\text{Translation along } Z_{t-1} \text{ axis}} \end{aligned} \quad (3)$$

$$\text{word} \mathbf{P}_i(t) = {}^w\mathbf{T}_0 \cdot {}^0\mathbf{T}_1 \cdot \dots \cdot {}^{t-1}\mathbf{T}_t \cdot \mathbf{P}_i \quad (4)$$

D. Mechanical Model of Drill Cutting Process

A mechanical model of the drill cutting force is built to establish the virtual sensor's transfer function from the image signal to the drilling force. This model comprehensively considers the cutting and indentation effect of the drill bit's major and chisel edge. With this mechanical model, many practical factors can be introduced, such as drill bit geometry, drilling speed, feed rate, and tissue material.

1) Cutting Force on the Major Edge: The cutting force on the major edge arises mainly from dual-sided edge cutting effects on the bone tissue, which are produced by the normal force F_n and the friction force F_f . As shown in Fig. 4(a), the drill

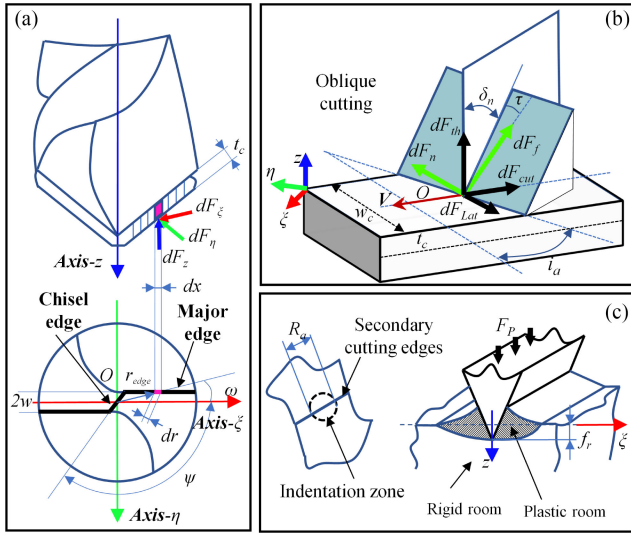


Fig. 4. Mechanical model of the drill cutting process. (a) Infinitesimal element model for the major cutting edges. (b) Oblique cutting model. (c) Chisel edge model of the secondary cutting edges and indentation zone.

bit cutting edge can be divided into infinitesimal edges. Each of the infinitesimal major edge cuttings can be considered a standard oblique cutting process. For this process (Fig. 4(b)), the infinitesimal normal force dF_n and friction force dF_f are proportional to the infinitesimal edge area dA_c . The proportional scale factor is related to the material characteristics, cutting thickness, cutting velocity, and cutting rake angle, which can be accurately modeled by the power law [25]. Equations (5) and (6) indicate the model of dF_n and dF_f , respectively.

$$dF_n = a_0 \cdot t_c^{a1} \cdot V^{a2} \cdot \delta_n^{a3} \cdot dA_c \quad (5)$$

$$dF_f = b_0 \cdot t_c^{b1} \cdot V^{b2} \cdot \delta_n^{b3} \cdot dA_c \quad (6)$$

where the cutting thickness t_c is determined by $t_c = 0.5f_r \sin \phi$ as a function of the feed rate f_r (ϕ is the half point angle of the drill bit). The cutting velocity V can be determined by $V = 2\pi \cdot N \cdot r_{edge} / 60$ as a function of the drill spindle speed N . Here, δ_n is the cutting rake angle, which is related to the drill bit geometric parameters [19]. Parameters $a_{0\sim 3}$ and $b_{0\sim 3}$ are correlation coefficients that can be obtained by the calibration method [22].

By decomposing the force in (5) and (6), the thrust force dF_{th} , the cutting force dF_{cut} , and the lateral force dF_{lat} of each infinitesimal element can be determined, as shown in Fig. 4(b). Using the geometric relationship between each infinitesimal element and the total drill bit, we can calculate the force and torque distribution in the drill bit coordinate frame represented as dF_z , dF_ξ , dF_η , and dM_z [19].

2) Cutting Force on the Drill Chisel Edge: The force on the drill bit chisel edge area can be divided into cutting force and indentation thrust force. As shown in Fig. 4(c), the central area of the chisel edge is deformed under the deformation thrust extrusion, while the other areas of the chisel edge still exhibit a cutting effect (secondary cutting area).

The secondary cutting area can also be modeled following oblique cutting of the major edge. The thrust force and torque on the indentation zone can be determined by (7) and (8), respectively, where k is the material yield strength, R_a is the deformation area radius, which is related to the feed rate and chisel edge point angle, δ_{nc} is the drill normal rake angle, and φ is a parameter related to the geometry of the drill bit. To simplify the calculation, only the thrust and torque are considered in the indentation zone, and the lateral force is ignored.

$$F_z = \frac{4k(1+\varphi)f_rR_a \sin \delta_{nc}}{\cos \delta_n - \sin(\delta_n - \varphi)} \quad (7)$$

$$M_z = \frac{2k(1+\varphi)f_rR_a^2 \cos \delta_{nc}}{\cos \delta_n - \sin(\delta_n - \varphi)} \quad (8)$$

3) Resultant Drill Force in the Inertial Coordinate System:

The above mechanical model establishes the force of the infinitesimal cutting element in the drill bit coordinate frame. Considering that the drill bit coordinate frame always rotates, the thrust and radial force under the drill bit coordinate can be further converted to a static global inertial coordinate frame to facilitate the measurement and analysis.

E. Image-Force Relationship Mapping

In the bone cutting process, the drill bit faces variations in bone shapes and bone material characteristics. The above drilling force model considered many factors but still lacks consideration of the time-varying cutting object shape and material characteristics. The image information of the target bone is introduced into the above drilling force model to further reflect the influence of the cutting object shape and material characteristics factors on the cutting force.

The oblique cutting normal force (5) and friction force (6) are weighted by the grayscale value of the CT images. Considering experimental studies have shown that bone materials' compressive strength and modulus have a power relationship with density [15], and the bone density is directly proportional to the CT value [13], [14]. The power of the CT grayscale is used to weigh the drilling force, which is also consistent with the viewpoint of the literature [18]. Equations (9) and (10) reveal the weighted personalized cutting normal force and friction force. Here, λ is the image gray value at the infinitesimal element's cutting position and μ is the power relationship coefficient. For the chisel edge indentation zone, λ^μ is also used for weighting.

$$dF_n = \lambda^\mu \cdot (a_0 \cdot t_c^{a1} \cdot V^{a2} \cdot \delta_n^{a3} \cdot dA_c) \quad (9)$$

$$dF_f = \lambda^\mu \cdot (b_0 \cdot t_c^{b1} \cdot V^{b2} \cdot \delta_n^{b3} \cdot dA_c) \quad (10)$$

The image gray value is normalized to eliminate the gray shift due to changes in CT tube voltage and device performance, and only the relative gray changes of the scanned object are considered. Equation (11) gives the normalization rule, which is determined as a piecewise linear function. Here, x represents the infinitesimal element's gray image value, which can be obtained by virtual sensors, and m_1 and m_2 represent normalized parameters, which can be determined according to the gray distribution characteristics of the image. Typically, for a drilled

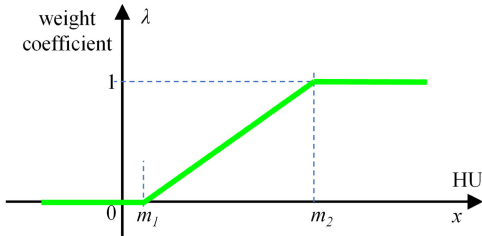


Fig. 5. Weight mapping rules from image CT values to force-material weight parameters λ .

bone object containing both cortical bone and cancellous bone, m_1 can be taken as the mean CT value of the cancellous bone area minus two times the standard deviation, and m_2 is the mean CT value of the cortical bone area plus two times the standard deviation. Fig. 5 vividly exhibits the normalization map from the gray image to the material parameters.

$$\lambda = \begin{cases} 0 & \text{if } x \leq m_1 \\ \frac{1}{m_2 - m_1} (x - m_1) & \text{if } m_1 < x < m_2 \\ 1 & \text{if } x \geq m_2 \end{cases} \quad (11)$$

F. Force Scale Normalization and Time Alignment

It is impossible to calibrate the model coefficient parameter separately for each patient, which makes it difficult to compare the magnitude of the drilling force calculated by different patient medical images. To solve this problem, we normalize the model's output force information based on the Z-axis thrust force. To unify the same time scale between the predicted and real force signals, time alignment is needed to determine the time alignment point and sampling frequency. The moment of contact between the drill bit and the bone surface is selected as the time alignment point of the predicted signal. For the model sampling frequency, by assuming N represents the spindle speed and n represents the force prediction model calculation times per revolution, the sampling frequency of the predicted signal can be determined by $Fre_{pre} = n \cdot N/60$.

III. RESULTS

In the results section, the model's response-ability is first tested in simulated data. Then, a real bovine bone and porcine bone drilling experiment are implemented to evaluate the model's accuracy. Finally, the constructed model is validated in a pedicle screw placement surgical plan to show the application potential.

A. Model Response Testing and Simulation

1) Drilling Force Response Under Different Grayscale Imagery:

A stepped pixel gray level image was designed to verify the model's response characteristics to different grayscale images. As shown in Fig. 6(a), the image gray value λ is divided into 10 step intervals from 0 to 1. The drilling path is controlled to be perpendicular to the target surface. Here, the model's correlation coefficients $a_{0\sim 3}$, $b_{0\sim 3}$, and the material

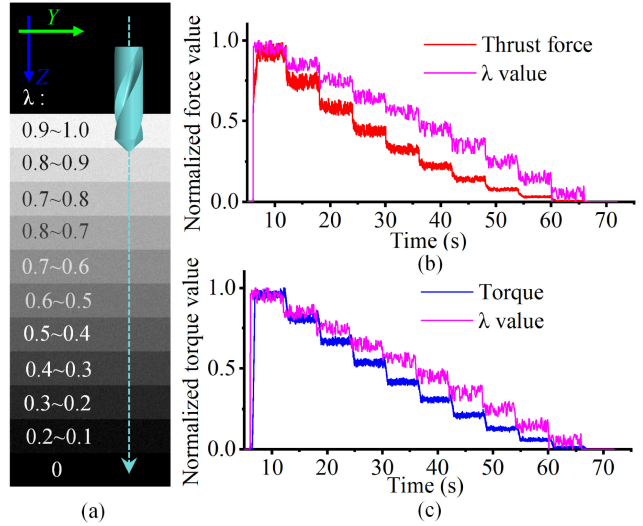


Fig. 6. Response of drilling force model output to image gray value. (a) Experimental schematic. (b) Thrust force curve during the experiment. (c) Torque curve during the experiment.

TABLE I
DRILLING MODEL COEFFICIENT PARAMETERS USED IN SIMULATION

| x | 0 | 1 | 2 | 3 |
|-------|-------|--------|--------|--------|
| a_x | 5.549 | 0.359 | 0.097 | 1.338 |
| b_x | 3.734 | -0.679 | -0.064 | -0.217 |
| k | | | 112.1 | |
| μ | | | 1.815 | |

yield strength k are derived from the research of Sui *et al.* [22]. The image-force weight relationship coefficient μ is derived from the research of Feldmann *et al.* [18]. Table I shows all parameters. These parameters are used in subsequent studies unless otherwise specified.

The relationship between the model's output thrust force, torque signal, and λ is shown in Fig. 6(b) and Fig. 6(c). To facilitate comparison, all results are normalized. We can find that the model's thrust force and torque signal output follow the change in λ , which maintains a good step shape. From (9) and (10), it can be deduced that the drop rate of the thrust force and torque is proportional to the change in λ^μ . This experiment shows that the output force information of the model can respond according to the gray value of the target image passed by the drilling path. The brighter the image the drill bit passes through, the greater the thrust and torque values output by the model, which is also in line with actual clinical experience.

2) Drilling Force Response Under Different Drilling Conditions and Drill Bit Geometry: We verify the model's responsiveness to drilling conditions and drill bit geometry parameters. As shown in Fig. 7(a), the bit is simulated to drill into a flat surface target with a uniform image feature ($\lambda = 1$).

For the drilling conditions, two commonly used factors, feed rate and spindle speed, are studied. Fig. 7(b) shows the thrust force and torque in the steady state under different feed rates at the spindle speed $N = 1000$ rpm. Fig. 7(c) shows the output thrust

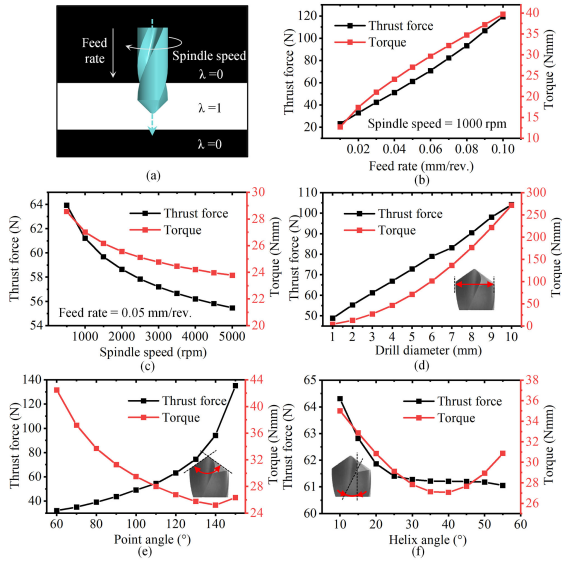


Fig. 7. Drilling force response under different drilling conditions and drill bit geometry. (a) Experimental schematic. (b)–(c) Model predictions of torque and thrust force curves under different cutting conditions. (d)–(f) Model predictions of torque and thrust curves under different drill bit geometries.

force and torque under different spindle speeds at feed rates $f = 0.05$ mm/rev. Under the selected parameters in Table I, our model predicts that the drilling thrust force and torque are proportional to the feed rate and inversely proportional to the spindle speed. This phenomenon is consistent with the actual drilling experiment results reported by another research group [24].

For drill bit geometry parameters, three drill bit geometry parameters, including drill bit diameter, point angle, and helix angle, are chosen. The results are shown in Fig. 7(d)–(f), where the drilling speed input by the model is 1000 rpm, and the feed rate is 0.05 mm/rev. The response trend of our model on the three main drill bit geometry factors of diameter (Fig. 7(d)), point angle (Fig. 7(e)), and helix angle (Fig. 7(f)) is consistent with the reported literature [24]. Therefore, we can conclude that the model can correctly respond to the force information changes brought by the drill bit geometry.

3) Drilling Force Response Under Inclined Drilling: We also tested the model output force response in an inclined drilling situation. As shown in Fig. 8(a), the drill bit passes through multiple inclined plane objects. Fig. 8(b) and Fig. 8(c) show the curves of the drilling thrust force and torque under different inclination angles. Fig. 8(d) and Fig. 8(e) show the radial force curves in the inertial coordinate frame. To facilitate comparison, all results are normalized as well. It can be found that the radial force curve given by the model not only reflects the amplitude change but also indicates the direction of the radial force. This information is useful when drilling into uneven bone surfaces.

B. Model Verification on the Real Bone Drilling Process

1) Materials and Experimental Design: Real bone drilling experiments were implemented to verify the consistency of the model. The experimental process is shown in Fig. 9(a). For a test

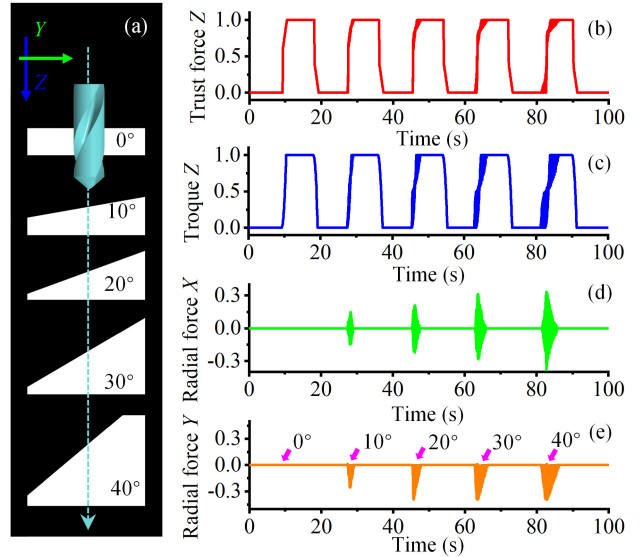


Fig. 8. Drilling force response under inclined drilling. (a) Experimental schematic. (b) Thrust force in the Z direction. (c) Z -axis torque. (d) Radial force in the X direction. (e) Radial force in the Y direction.

bone block, a CT scan was first performed before drilling. Then, after the drilling is completed, the bone block was subjected to a CT scan again. Through the registration of the bone block CT images before and after drilling, an accurate drilling path in image space could be obtained. The drilling path, together with the bone block preoperative 3D image, real drilling spindle speed, feed rate, and drill bit geometry information was incorporated into our models. The model prediction force information was compared with the real measurement force information, which evaluates the model's consistency.

Fig. 9(b) shows a schematic diagram of the bone drill experiments. Here, MicroCT (Quantum GX MicroCT, PerkinElmer Inc., USA) was used for bone block CT scanning. The output image size was $512 \times 512 \times 512$, with a 0.144 mm voxel size, 90 kV tube voltage, and 88 mA tube current, as shown in Fig. 9(c). The drilling equipment was a self-constructed three-coordinate line drilling system, as shown in Fig. 9(d). The theoretical motion resolution of this system was 1.6 μ m. The electric drill was driven by a DC geared motor (RE40 148877, Maxon Motor Co., Ltd, Switzerland) with a maximum speed of 3000 rpm. The spindle speed was adjusted by a servo controller. The sampling rate of the force sensor (DynPick WEF-6A200N-4-RCD, Wacoh Tech, Japan) was 2 kHz.

The drilling experiment was carried out on bovine and porcine rib bone blocks. The diameter of the drill bit was chosen from 2 mm, 3 mm, and 4 mm. The spindle speed was chosen from 500 rpm, 1000 rpm, and 1500 rpm. The feed rate was chosen from 0.02 mm/rev., 0.04 mm/rev. and 0.06 mm/rev. A total of 15 bovine bone drilling paths and 12 porcine bone drilling paths were collected. On the bovine bone, to obtain the prediction force with true amplitude, we first extracted three bovine bone drilling paths (B-Path1, B-Path8 and B-Path14) and used the method in [22], [23] to recalibrate the parameters in Table I. Using the calibrated parameters, we predicted all bovine bone

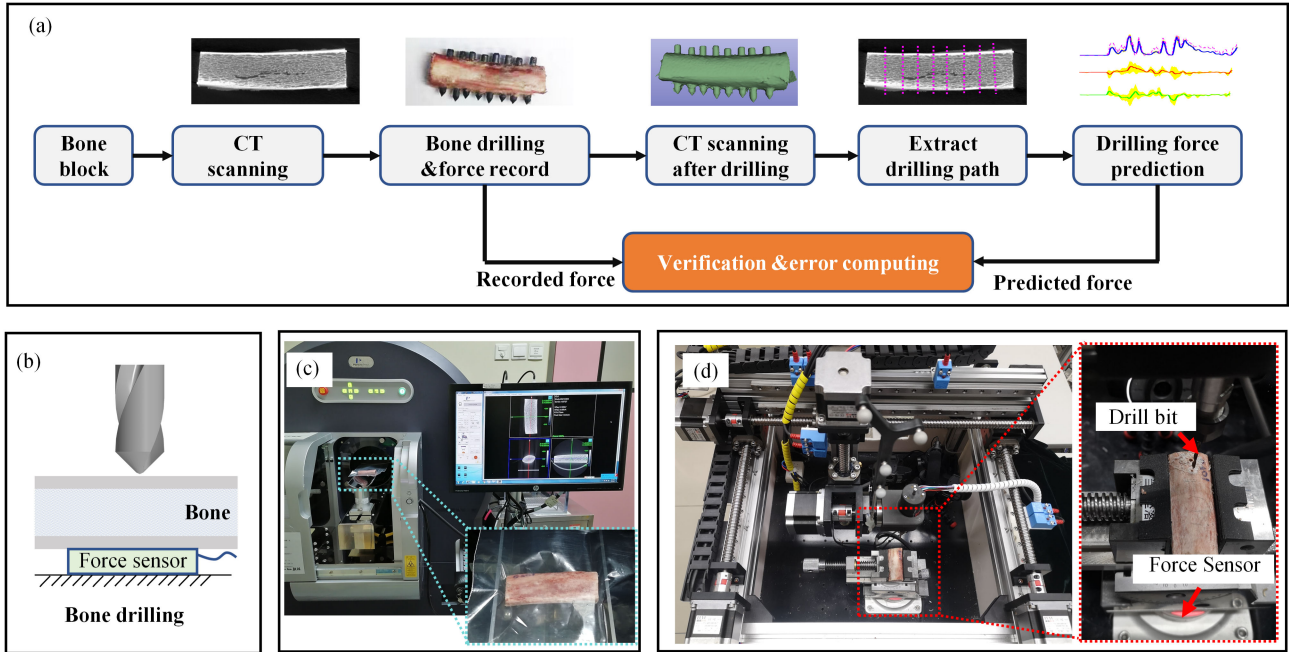


Fig. 9. Model verification on real bone drilling experiments. (a) Schematic diagram of the verification experiment. (b) Schematic diagram of drilling force information collection. (c) Micro CT scanning process. (d) Bone drilling and force signal acquisition device platform.

drilling paths. On porcine bone, to verify the adaptability of the method to different bone materials, we directly used the calibrated parameters on bovine bone to predict the force information and then compared the predicted and recorded forces after normalization.

When drilling deep holes, the chip-clogging phenomenon may occur. At this time, the drill cutting process is disturbed, and the drilling force rises sharply [26]. To prevent this phenomenon from affecting the evaluation results, we exclude the force information of the 3 mm length before the drilling breakthrough.

Considering that the drill bit is nearly perpendicular to the bone surface during drilling, the radial cutting force amplitude is small, and the radial force measured by the actual force sensor is greatly disturbed by the noise of the drill bit installation error. This experiment uses the thrust force signal for model verification only.

2) Evaluation and Analysis of Experimental Results:

The signal error at each sampling point (point-by-point error) after the signal time alignment is used to evaluate the model's accuracy. The mean value of the point-by-point error represents the overall prediction accuracy on the drilling path, and the standard deviation of the point-by-point error represents the volatility of the force prediction accuracy.

Fig. 10 shows the evaluation results of the model's prediction accuracy. Fig. 10(a) and Fig. 10(b) show the two best prediction paths on the bovine bone (B-Path3 and B-Path12). The light purple and pink curves are the original information for sensor recording and model prediction, respectively, the blue and red curves are the corresponding smoothing filtering results for recording and prediction force, respectively, and the gray dotted line is the CT image signal where the drill tip passes through on virtual image space. According to the statistics, after

ignoring the interference of the chip-clogging phenomenon, the prediction errors of paths B-Path3 and B-Path12 are 1.64 ± 1.49 N and 1.13 ± 0.95 N, respectively. Fig. 10(c) shows the worst prediction result (B-Path5) on bovine bone, with a prediction error of 3.61 ± 3.97 N.

On the porcine bone drilling path, we normalized the predictive force and the measured force and used relative values for evaluation. Fig. 10(d) and Fig. 10(e) show the two best prediction results on porcine bones (P-Path3 and P-Path9). The normalized prediction errors of P-Path3 and P-Path9 are 0.11 ± 0.07 and 0.07 ± 0.08 , respectively. Fig. 10(f) shows the worst prediction result (P-Path7) on porcine bones, with a normalized prediction error of 0.16 ± 0.16 . Fig. 10(g) shows the error mean and standard deviation distributions of all bovine bone drilling paths. Fig. 10(h) shows the normalized mean and standard deviation distributions of all porcine bone drilling paths.

For the calculation time, the model is run on MATLAB 2020b software, and the calculation hardware is Microsoft Surfacebook 2 (CPU: Intel Core i7 8650U, 2.11 GHz). The number of microelements on one side of the drill bit is set to 100, and the model calculation frequency is ten times per drill bit revolution. The total calculation time for all 15 bovine bone paths is 146.7 s, and each path takes 9.7 s on average. The total calculation time of the 12 bovine bone paths is 88.6 s, and the average time for each path is 7.4 s.

The force information predicted by the model is in good agreement with the actual measurements, both on bovine bones and on porcine bones. The model gives thrust force predictions that are nearly consistent with the real sensor measured values on the calibrated bovine bone drilling model parameters. After normalization, the model also showed a thrust force prediction trend consistent with the measured value on the porcine bone. Note

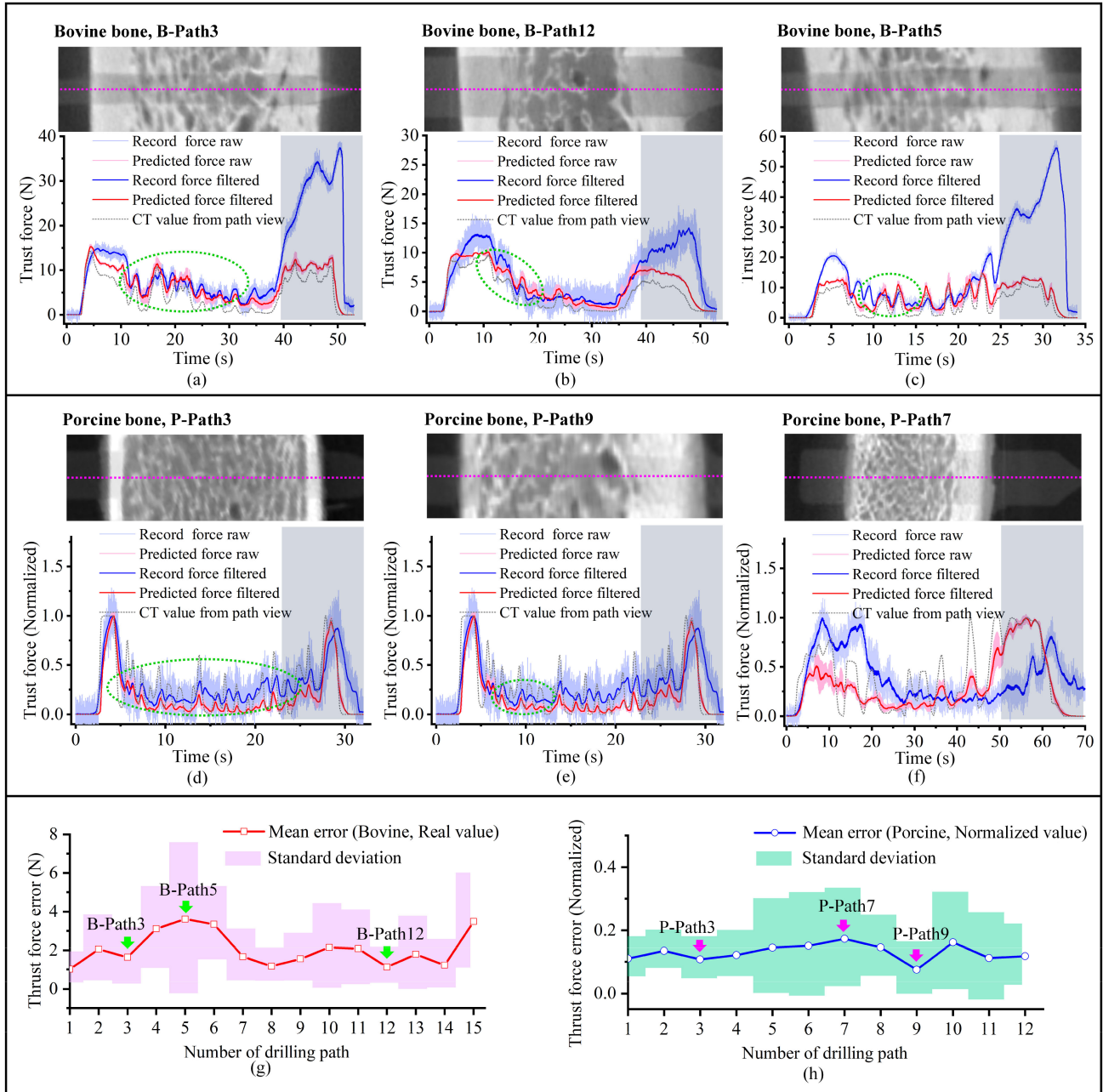


Fig. 10. Comparison of typical model predictive force and actual measurement force. (a)–(b) Best two prediction paths on bovine bone. The upper part is the CT image of the drilling path area registered before and after drilling, and the lower part is the comparison between the predicted force and the measurement force. The gray area is the part where chip clogging may occur, which is excluded from the evaluation calculation. (c) Worst prediction path on the bovine bone. (d)–(e) Best two prediction paths on the porcine bone. (g) Error distribution of all paths on the bovine bone, the green arrow marks the path shown in (a)–(c); (h) Normalized error distribution of all paths on the porcine bone. The pink arrows mark the paths shown in (d)–(f).

that the model's material parameters used in the porcine bone are calibrated with bovine bone, which shows that the tissue's CT image can provide enough material parameter information for the model to predict the trend of drilling force. This means that material coefficient parameter calibration may not necessarily be essential if we wish to know only the trend of the drilling force instead of the specific value.

In addition to the general trend consistency, it can also be observed in Fig. 10 that the predicted force given by the model

is also quite consistent with the sensor measured value in detail. We selected some typical areas and marked them with green elliptical dotted frames in Fig. 10.

C. Model Verification on Real Surgical Image

The method was further tested in pedicle screw placement surgery images. Fig. 11 shows the force prediction results for a pedicle screw placement surgical plan on one side of a lumbar

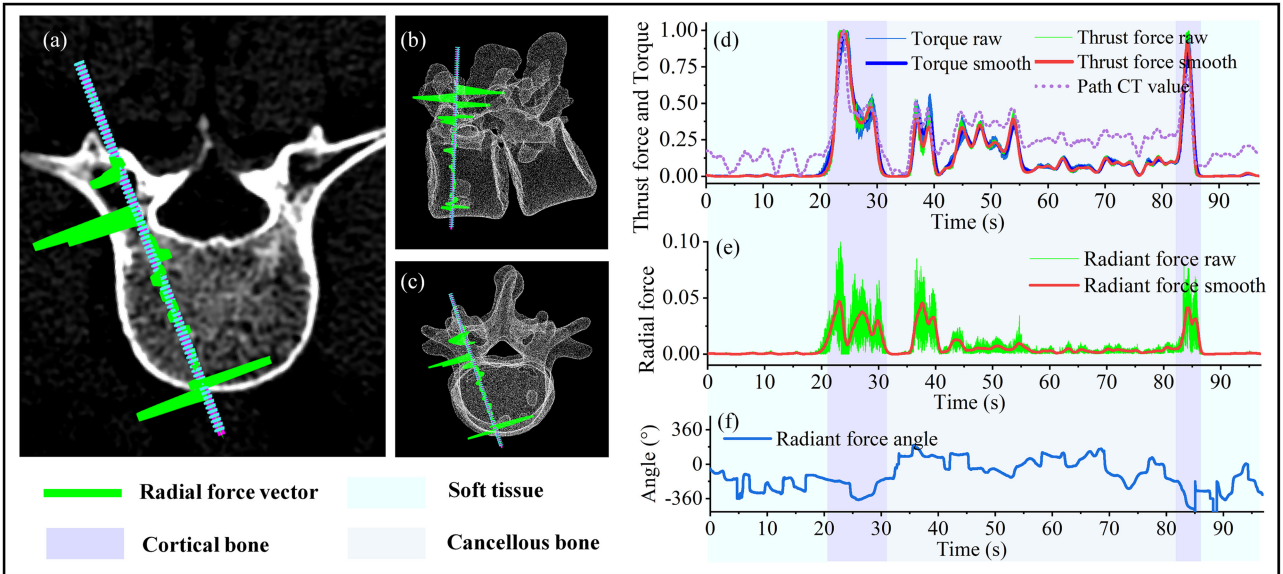


Fig. 11. Visualization of the predicted force information in the pedicle screw placement surgery plan. (a)–(c) Preoperative surgery plan and radial force vector distribution under different perspectives. (d) Predicted thrust force, torque and path CT value curve (normalized value). (e) Normalized radial force curve. (f) Radial force angle distribution.

spine L3 segment. The image pixel size is 0.3 mm, the drilling diameter is 3 mm, the feed rate is 0.05 mm/rev., and the spindle speed is 1000 rpm. Fig. 11(a) visualizes the radial force vector (green line) distribution with the anatomical image structure under a surgical path. Fig. 11(b) and Fig. 11(c) show the predicted lateral forces from the other two viewpoints. Fig. 11(d)–(f) shows the normalized thrust force, torque, radial force, and radial force angle curves predicted by the model under this planning path, where the color blocks indicate the different anatomical tissue areas corresponding to the force signals.

Fig. 11(d)–(f) clearly shows that for this planned drilling path, when the drill bit contacts the cortical bone, a larger thrust force, and torque are generated. A certain lateral force is also generated at the same time. When the drill bit enters the bone tissue, the thrust and lateral force are maintained at a low amplitude. If the drill bit continues to feed, when it is about to break through the second cortical bone of the vertebral body, it generates a large thrust and lateral force again. This feature provides alarm information for the drill bit feed, which should be absolutely avoided during the robot drilling process.

IV. DISCUSSION

In this work, preoperative images were introduced to predict bone drilling force information. By combining a virtual sensing framework and drilling process mechanical models, various factors, such as the shape of the drilling object, material properties, drilling conditions, and drill bit geometry, can be comprehensively considered to predict the thrust force, torque, and radial force, which can provide a priori operating force information for robotic drilling operations. The method was tested in both simulated and real bone drilling (bovine and porcine) environments. The results show that the predicted drilling force

can respond well to various factors and can also predict the thrust force change trend during the drilling process.

The matrix data form 2D or 3D visual images is very suitable for human visual observation habits. However, for robot observation and computing, it deserves more efficient image processing method. In this paper, we present a possibility that allows us to use virtual sensors to focus only on the contact area between the cutting tool effective part and the tissue anatomy image. The 2D or 3D imagery information can be reduced to a one-dimensional signal. After some mathematical model calculations, this one-dimensional information can be converted into a form consistent with the sensor signal (such as cutting force signal), which is an easier process for robots. We believe that the virtual sensor concept used in this paper is an important perspective for observing image information.

In bone drilling, the uneven bone surface makes it difficult to ensure that the drill bit is perpendicular to the bone surface, and the bone tissue material properties of different parts are also inconsistent. Therefore, the shape and material of the target object must be considered during bone drilling, and the drill force contains not only thrust force but also radial force. This paper presents a model that considers the factors of uneven bone surfaces and inconsistent bone materials. According to (9) and (10) and Fig. 4, the uneven bone surface factor is reflected in the unbalanced contact area of the cutting edges on both sides of the drill bit, while the bone material properties factor is characterized by CT images. This design expands the model's ability to deal with cutting target's shapes and material properties, and to couple the final impact of both factors to the model's output thrust force and radial force, providing a more realistic bone drilling process model to make it easier for robots to obtain a preoperative awareness of the drilling process situation.

In real bone drilling experiments, the calculation time of our method on each path is less than 10 s. The time consumption mainly comes from the large number of spatial and temporal microelement calculations. Theoretically, the finer these microelements are, the longer the planned surgical path and the more calculation time is required. For our method to be applied to surgery robots, short time consumption is not urgently needed because the model is mainly used to predict prior information that can be calculated before the operation. For real-time application scenarios that require higher computing efficiency, more efficient language and parallel computing can be introduced for large quantities of microelement calculations to further reduce the calculation time.

The setting of imaging parameters has an important influence on the model. The CT grayscale is proportional to bone density, while the proportional slope is determined by the tube voltage [27]. This leads to contrast differences in the imaging grayscale of the same tissue density under different CT tube voltages. We normalize the image grayscale to avoid this problem. In this way, we do not need to consider the influence of CT tube voltage. But this also means that we cannot obtain the absolute density of the target through the CT image. Therefore, without the calibration step, only the trend information of the drilling force can be obtained. However, the trend information is still valuable for robot drilling status identification studies [16], [28].

The image voxel resolution (voxel size) is also important. In the model, we divide the cutting edge and spatial motion of the drill bit into microelements for calculation. The division fineness of the microelements is highly related to the CT voxel size. The calculation of microelement motion that is much smaller than the voxel size is meaningless because it is equivalent to performing multiple calculations in the same voxel, which results in exactly the same calculation results and increases the calculation time. Conversely, if the voxel size is too large, the fineness of the model's response abilities to the material and shape factors is affected. When the voxel size is very large (For example 1.5 mm) and the size of the drill bit is small (For example 2 mm), the cutting edge of the drill bit can pass only one or two voxels at a time. These one or two voxels can hardly reflect the shape and material changes of the anatomical structure on the drilling contact area. Thus, for the use of our model, the voxel size of CT image was supposed to be as fine as possible, and much smaller than the drill bit geometric size. Moreover, the division size of the microelement also should be comparable to the voxel size, which is neither too small nor too large. An appropriate image interpolation method may be helpful for obtaining smaller voxel pixels, which can ensure that the method obtains the calculation result, but how much the prediction performance is affected by the interpolation operation still needs further evaluation.

The interaction relationship between the drill bit and bone tissue is very complicated. Although the method in this paper considers many factors, there are still many practical situations that need further consideration. In the curves of Fig. 10(a)–(c), the recorded force in the later stage of the drilling process is much larger than the predicted force. This is caused by the chip-clogging phenomenon in deep hole drilling [26]. The proposed model does not consider this phenomenon, which is

the cause of the deviation. In addition, the deformation of the drill bit and the slip factor when in contact with the bone surface also affect the consistency of the amplitude and phase between the actual measurement and the model prediction signal. In the practical application of the model, we need to pay attention to the possible impact of these unmodeled factors. Moreover, we can also consider combining more modal information to incorporate these factors into the model for predicting drilling force information better.

V. CONCLUSION

This work aims to model a robot drilling process combined with image information to help robots preoperatively predict drilling force information. The proposed model incorporates many practical factors, such as the shape of the drill object, material characteristics, cutting conditions, and drill bit geometries. The model has a good response to the considered practical factors and can predict the trend of the thrust change during the drilling process. This study provides an information basis for the automatic operation of surgery robots and provides a more inspirational perspective to study the interaction relationship between surgical instruments and tissues with the assistance of preoperative images.

REFERENCES

- [1] M. Jamil *et al.*, "Comprehensive analysis on orthopedic drilling: A state-of-the-art review," *Proc. Inst. Mech. Eng. Part H-J. Eng. Med.*, vol. 234, no. 6, pp. 537–561, Jun. 2020.
- [2] C. Faria, W. Erlhagen, M. Rito, E. De Momi, G. Ferrigno, and E. Bicho, "Review of robotic technology for stereotactic neurosurgery," *IEEE Rev. Biomed. Eng.*, vol. 8, pp. 125–137, 2015.
- [3] A. Khan *et al.*, "Next-generation robotic spine surgery: First report on feasibility, safety, and learning curve," *Oper. Neurosurgery*, vol. 17, no. 1, pp. 61–39, 2018.
- [4] M. Lefranc *et al.*, "Frameless robotic stereotactic biopsies: A consecutive series of 100 cases," *J. Neurosurg.*, vol. 122, no. 2, pp. 342–352, Feb. 2015.
- [5] F. R. Ong and K. Bouazza-Marouf, "The detection of drill bit breakthrough for the enhancement of safety in mechatronic assisted orthopaedic drilling," *Mechatronics*, vol. 9, no. 6, pp. 565–588, Sep. 1999.
- [6] M. Louredo *et al.*, "DRIBON: A mechatronic bone drilling tool," *Mechatronics*, vol. 22, no. 8, pp. 1060–1066, Dec. 2012.
- [7] T. Boiadjiev *et al.*, "Far cortex automatic detection aimed for partial or full bone drilling by a robot system in orthopaedic surgery," *Biotechnol. Biotechnol. Equip.*, vol. 31, no. 1, pp. 200–205, 2017.
- [8] V. Zakeri and A. J. Hodgson, "Automatic identification of hard and soft bone tissues by analyzing drilling sounds," *IEEE-ACM Trans. Audio Speech Lang.*, vol. 27, no. 2, pp. 404–414, Feb. 2019.
- [9] Y. Sun, H. Jin, Y. Hu, P. Zhang, and J. Zhang, "State recognition of bone drilling with audio signal in robotic orthopedics surgery system," in *Proc. IEEE Int. Conf. Intell. Robots Syst.*, 2014, pp. 3503–3508.
- [10] Y. Dai, Y. Xue, and J. Zhang, "Milling state identification based on vibration sense of a robotic surgical system," *IEEE Trans. Ind. Electron.*, vol. 63, no. 10, pp. 6184–6193, Oct. 2016.
- [11] P. Puangmali *et al.*, "Sensorless stepwise breakthrough detection technique for safe surgical drilling of bone," *Mechatronics*, vol. 65, pp. 1–9, Feb. 2020.
- [12] Y. Torun and A. Ozturk, "A new breakthrough detection method for bone drilling in robotic orthopedic surgery with closed-loop control approach," *Ann. Biomed. Eng.*, vol. 48, no. 4, pp. 1218–1229, Apr. 2020.
- [13] C. Meghan *et al.*, "Repeatable calibration of hounsfield units to mineral density and effect of scanning medium," *Adv. Biomech. Appl.*, vol. 1, no. 1, pp. 15–22, 2014.
- [14] J. J. Schreiber *et al.*, "Hounsfield units for assessing bone mineral density and strength: A tool for osteoporosis management," *J. Bone Joint Surg.-Amer.*, vol. 93A, no. 11, pp. 1057–1063, Jun. 2011.

- [15] A. Wall and T. Board, "The compressive behavior of bone as a two-phase porous structure," in *Classic Papers in Orthopaedics*, P. A. Banaszkiewicz and D. F. Kader, eds., London, U.K.: Springer, 2014, pp. 457–460.
- [16] H. Y. Jin *et al.*, "Model-based state recognition of bone drilling with robotic orthopedic surgery system," in *Proc. IEEE Int. Conf. Robot. Automat. ICRA*, 2014, pp. 3538–3543.
- [17] T. M. Williamson *et al.*, "Estimation of tool pose based on force-density correlation during robotic drilling," *IEEE Trans. Biomed. Eng.*, vol. 60, no. 4, pp. 969–976, Apr. 2013.
- [18] A. Feldmann *et al.*, "Temperature prediction model for bone drilling based on density distribution and in vivo experiments for minimally invasive robotic cochlear implantation," *Ann. Biomed. Eng.*, vol. 44, no. 5, pp. 1576–1586, May 2016.
- [19] Y. P. Gong *et al.*, "Dynamics of initial penetration in drilling: Part 1 - Mechanistic model for dynamic forces," *J. Manuf. Sci. Eng.-Trans. ASME*, vol. 127, no. 2, pp. 280–288, May 2005.
- [20] Y. P. Gong *et al.*, "Dynamics of initial penetration in drilling: Part 2 - Motion models for drill skidding and wandering with experimental verification," *J. Manuf. Sci. Eng.-Trans. ASME*, vol. 127, no. 2, pp. 289–297, May 2005.
- [21] R. S. Anand *et al.*, "Mechanistic modeling of micro-drilling cutting forces," *Int. J. Adv. Manuf. Technol.*, vol. 88, no. 1–4, pp. 241–254, Jan. 2017.
- [22] J. Sui *et al.*, "Mechanistic modeling of bone-drilling process with experimental validation," *J. Mater. Process. Technol.*, vol. 214, no. 4, pp. 1018–1026, Apr. 2014.
- [23] J. Lee *et al.*, "Modeling and experimentation of bone drilling forces," *J. Biomech.*, vol. 45, no. 6, pp. 1076–1083, Apr. 2012.
- [24] J. B. Sui and N. Sugita, "Experimental study of thrust force and torque for drilling cortical bone," *Ann. Biomed. Eng.*, vol. 47, no. 3, pp. 802–812, Mar. 2019.
- [25] P. L. B. Oxley, "Rate of strain effect in metal cutting," *J. Eng. Ind.*, vol. 85, no. 4, pp. 335–337, 1963.
- [26] A. R. Zhang S. Zhang, C. Bian, and H. Kong, "Modified chip-evacuation force modeling and chip-clogging prediction in drilling of cortical bone," *IEEE Access*, vol. 7, pp. 180671–180683, 2019.
- [27] M. B. Afifi *et al.*, "The effects of CT X-ray tube voltage and current variations on the relative electron density (RED) and CT number conversion curves," *J. Radiat. Res. Appl. Sci.*, vol. 13, no. 1, pp. 1–11, 2020.
- [28] Y. Hu, H. Jin, L. Zhang, P. Zhang, and J. Zhang, "State recognition of pedicle drilling with force sensing in a robotic spinal surgical system," *IEEE-ASME Trans. Mechatron.*, vol. 19, no. 1, pp. 357–365, Feb. 2014.